

## Article

# Effect of Heat Treatment on Microstructure and Properties of GH3536 Fabricated by Selective Laser Melting

Shuai Huang<sup>1</sup>, Bingqing Chen<sup>1</sup>, Wei Liu<sup>1</sup>, Biao Zhou<sup>1</sup>, Xuejun Zhang<sup>1</sup>, Qi Zeng<sup>2,3</sup> and Shaoqing Guo<sup>1,\*</sup>

<sup>1</sup> 3D Printing Research and Engineering Technology Center, Beijing Institute of Aeronautical Materials, Beijing 100095, China; hshuai987@buaa.edu.cn (S.H.); hwtkjcbq1984@163.com (B.C.); liuwei2011621@sina.com (W.L.); zhoubiao0317@163.com (B.Z.); zhangxuejun621@163.com (X.Z.)

<sup>2</sup> AECC Hunan Aviation Power Plant Research Institute, Zhuzhou 412002, China; 12024082@zju.edu.cn

<sup>3</sup> School of Aeronautics and Astronautics, Zhejiang University, Hangzhou 310027, China

\* Correspondence: gsq0046@sina.com

**Abstract:** Selective laser melting (SLM) forming technology to prepare nickel-based superalloy parts can significantly save costs and solve bottleneck problems. The extremely high-temperature gradient and large residual stress during SLM lead to structural defects and compositional segregation. The parts formed by SLM urgently need heat treatment to control the microstructure composition and improve mechanical properties. Results showed that the heat treatment did not significantly change the microcracks and pores in the SLM sample, but the carbides in the grain boundary gradually changed from a granular distribution to a continuous strip distribution. After heat treatment, the elongation increased significantly, but the yield strength decreased. The tensile fracture of the SLM samples changed from a transgranular fracture to a ductile fracture, and obvious plastic deformation occurred, confirming that heat treatment can improve the benefits of the SLM sample.



**Citation:** Huang, S.; Chen, B.; Liu, W.; Zhou, B.; Zhang, X.; Zeng, Q.; Guo, S.

Effect of Heat Treatment on Microstructure and Properties of GH3536 Fabricated by Selective Laser Melting. *Metals* **2022**, *12*, 1184. <https://doi.org/10.3390/met12071184>

Academic Editor: Evgeny A. Kolubaev

Received: 23 June 2022

Accepted: 9 July 2022

Published: 12 July 2022

**Publisher's Note:** MDPI stays neutral with regard to jurisdictional claims in published maps and institutional affiliations.



**Copyright:** © 2022 by the authors. Licensee MDPI, Basel, Switzerland. This article is an open access article distributed under the terms and conditions of the Creative Commons Attribution (CC BY) license (<https://creativecommons.org/licenses/by/4.0/>).

**Keywords:** selective laser melting; GH3536; microstructure; heat treatment

## 1. Introduction

Selective laser melting (SLM), as a kind of additive manufacturing technology, uses a laser as a heat source to achieve a high-quality metal powder layer by point-by-point melting, line-by-line overlap, and layer-by-layer solidification [1–3]. It has many advantages, such as saving raw materials, not being limited by the complexity of the shape, not requiring molds, and having a short preparation cycle. It is suitable for the manufacture of parts with complex shapes and high precision [4–6].

GH3536 alloy is a nickel-based superalloy (corresponding to Hastelloy-X) and its main strengthening elements are Cr and Mo [7–9]. The alloy has excellent durability, creep resistance, high-temperature stability below 900 °C, and the short-term working temperature can be as high as 1080 °C [10]. It is mainly used to make hot-end components and high-temperature gas-cooled reactors. However, these components are complex in shape, and there are often flow channels or porous structures inside. Traditional processes are mostly made by welding multiple composites, which is not only difficult to ensure dimensional accuracy, but also affects the stability of gas flow [11]. The use of SLM forming technology to prepare GH3536 alloy components can significantly save costs and solve the bottleneck problem [12–14].

The current research on the SLM of GH3536 alloy mainly focuses on the optimization of process parameters, defect control, and microstructure evolution [15–20]. There are significant differences in structure between SLM-formed alloys and traditionally processed alloys. Han et al. [21] found that adding 1 wt.% TiC nanoparticles in the GH3536 powder can not only increase the ratio of sub-grain and small-angle grain boundaries in the structure, but also eliminate hot cracks in the deposited parts. Tensile strength and yield strength at room temperature increased by 98 and 115 MPa, respectively. Wang et al. [15] studied

the formed GH3536 and hot isostatic pressing (HIP) treatment and found that the HIP treatment could close voids in the SLM alloy and improve the ultimate fatigue strength of formed parts.

During the SLM forming process, alloy powder needs to be melted, solidified, and cooled within an extremely short time. The high-temperature gradient caused by the localized heat input and the large residual stress generated during the solidification process will lead to structural defects of the alloy. Therefore, the SLM forming parts usually need post-heat treatment to repair the internal defects, control the composition and microstructure, and improve mechanical properties.

## 2. Experimental Details

Gas-atomized spherical GH3536 alloy powders were used as raw materials for SLM deposition. GH3536 alloy (Cr: ~20.4 at%, Mo: ~10.1 at%, Fe: ~17.0 at%, and Ni) powder is mainly spherical and the particle size range is 20~40  $\mu\text{m}$  with an approximately normal particle size distribution.

The equipment uses a solid fiber laser as the laser source, the maximum laser power is 400 W, the effective forming size is 250 mm  $\times$  250 mm  $\times$  325 mm, the scanning speed is 1000 mm/s, the scanning spacing is 0.11 mm, the slice layer thickness is 40  $\mu\text{m}$ , and the thickness of the substrate is 40  $\mu\text{m}$ . The size of the tensile samples is  $\Phi$  13.5  $\times$  73 mm and the diameter of the work section is  $\Phi$  13.5 mm.

The substrate for forming is 316 stainless steel, the size is 250 mm  $\times$  250 mm  $\times$  30 mm, the preheating temperature is 100  $^{\circ}\text{C}$ , and the whole preparation process is carried out in an Ar atmosphere. After SLM forming, these samples are separated from the substrate by wire cutting, which is recorded as the as-deposited sample (SLMed sample). The SLMed GH3536 was kept at 1130  $^{\circ}\text{C}$  for 2 h and air-cooled to room temperature; these samples are recorded as heat treatment samples (HTed sample) [22].

Due to the process characteristics of SLM, the SLMed GH3536 tends to have microstructure and properties in the forming direction: building direction (defined as a longitudinal direction, longitudinal sample), laser scanning direction (defined as transverse direction, transverse sample), and 45 $^{\circ}$  direction (45 $^{\circ}$  sample), as shown in Figure 1. The microstructure of SLMed GH3536 in different directions is observed, and mechanical properties are measured according to GB/T 228.2-2015. The temperature of the tensile tests is 815  $^{\circ}\text{C}$  and the tensile speed is 1 mm/min.

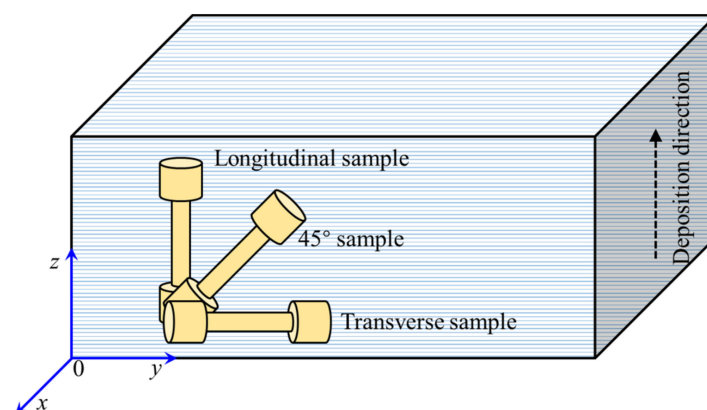


**Figure 1.** Tensile samples and sampling location.

## 3. Results and Discussion

### 3.1. Macroscopic Morphology before and after Heat Treatment

To observe pores and cracks inside the sample in three directions, samples were ground and polished. Figure 2a–c shows the morphology of the SLMed samples. There were many pores formed by unfused regions between scan lines inside the sample; some cracks spread along the grain boundary. Since the grain boundary was a post-solidification

area when the liquid metal was insufficiently fed, thermal cracks were easily generated at the grain boundary, and the bonding at the grain boundary was weak. Under the action of thermal stress, the crack was easily spread along the grain boundary and increased form failure.

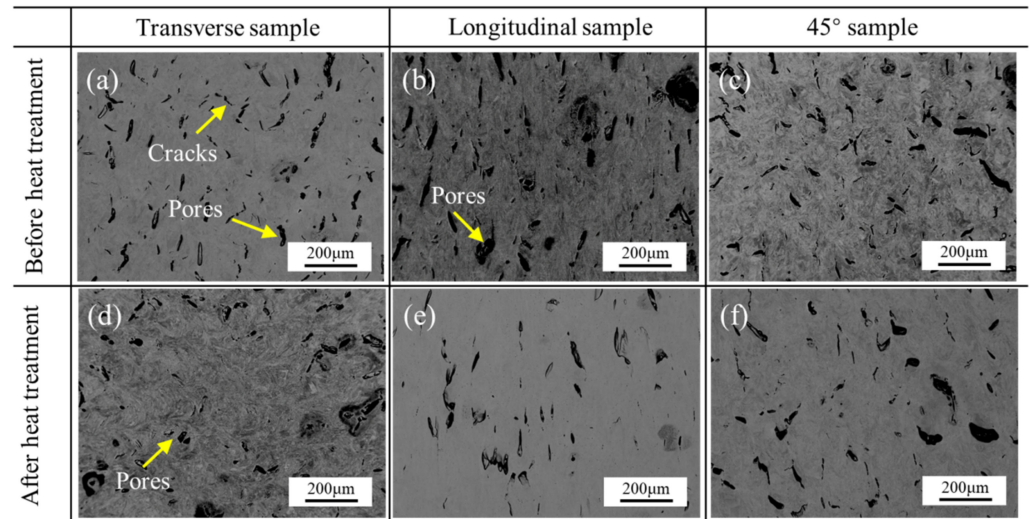


**Figure 2.** Surface morphologies of SLM GH3536 alloy samples before (a–c) and after (d–f) heat treatment in different directions.

In addition, there were closed pores in the SLM sample. The pores originated from the voids left between alloy powders during the spreading process. When SLM occurred, the gas remaining in these voids failed to escape from the rapidly solidified melt in time. The huge temperature gradient generated during the rapid solidification and cooling of the melt caused micro-cracks to appear when the residual stress exceeded the maximum tensile strength [23]. The number of pores and cracks in each direction did not change significantly after heat treatment, the heat treatment had little effect on it, and the effect was limited, as shown in Figure 2d–f.

### 3.2. Mechanical Properties before and after Heat Treatment

Figure 3 shows the mechanical properties of the SLMed and HTed GH3536. The tensile strength, elongation, and area contraction of the transverse sample, 45° sample, and longitudinal sample increased in turn, while the yield strength did not change significantly. The cold-rolled GH3536 sheet formed by the conventional processing had a tensile yield strength of 310 MPa, a tensile strength of 725 MPa, and an elongation of 35% at room temperature. The maximum tensile strength of the SLMed samples was 778 MPa (longitudinal samples) and the maximum yield strength was 578 MPa (transverse samples). The comprehensive mechanical properties of transverse specimens were weaker than those of longitudinal specimens, and the mechanical properties were anisotropic. The difference between the transverse and longitudinal microstructures of samples was the main reason for the difference in the tensile properties [24].

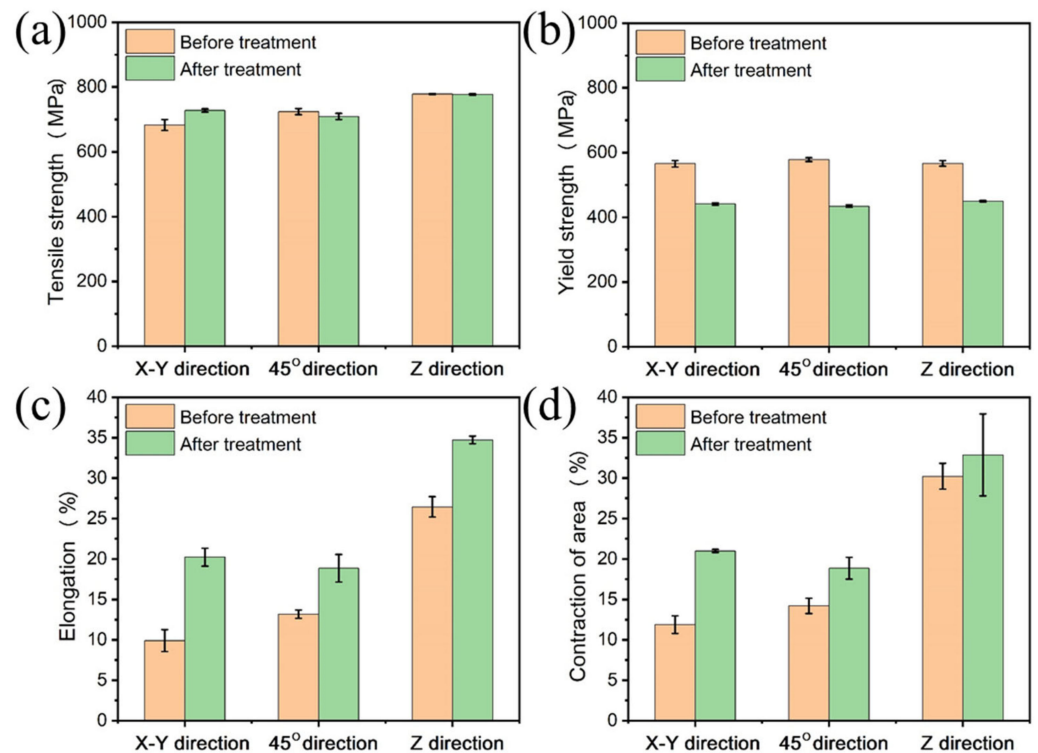


**Figure 3.** Room-temperature tensile properties of samples before and after heat treatment: (a) tensile strength; (b) yield strength; (c) elongation; and (d) the contraction of area.

After heat treatment, the tensile strength did not change significantly, the yield strength decreased obviously, and the elongation and area contraction increased significantly. Continuously distributed carbides were precipitated at the grain boundary which increased the grain boundary strength and increased the high-temperature elongation. It could be seen that the morphology of grain boundary carbides had a great influence on the elongation of GH3536 alloy.

The high-temperature tensile test was carried out according to the GB/T 228.2-2015 standard, and the mechanical properties at 815 °C of different samples were obtained. Figure 4 shows the histogram of the high-temperature mechanical properties of samples. The tensile strength and yield strength of SLMed GH3536 at 815 °C were higher than those of HTed GH3536, but the elongation after fracture and the contraction of the area of the former were significantly lower than those of the latter. SLMed samples had high strength and poor shaping. The grain size of the SLMed sample was much smaller than that of the hot-rolled sample, which was the main reason that the tensile strength of the former at 815 °C was higher than that of the latter. The carbides dissolved into the matrix at high temperatures, and the carbides in the matrix dissolved uniformly. During cooling, the carbide precipitation temperature range stayed for a long time and the precipitation kinetic energy was large. Therefore, more continuous carbides were precipitated at the grain boundary, which played a role in the grain boundary. The effect of strengthening and the high-temperature elongation had been significantly improved.

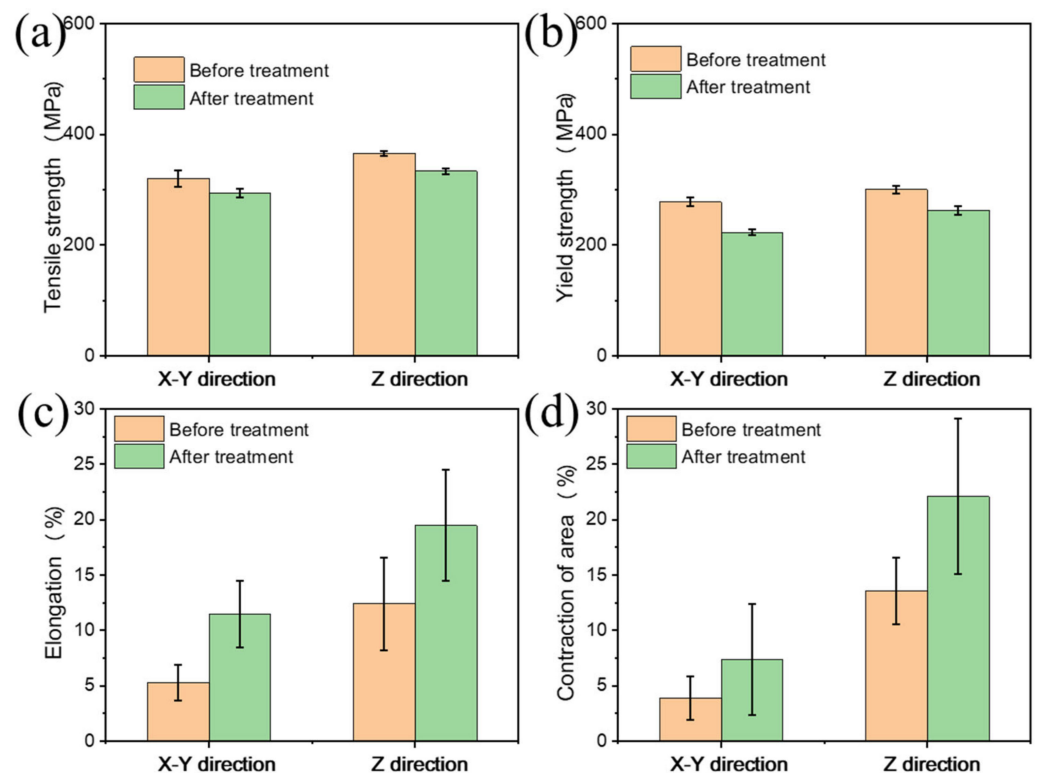


**Figure 4.** High-temperature tensile properties of samples before and after heat treatment: (a) tensile strength; (b) yield strength; (c) elongation; and (d) the contraction of area.

### 3.3. Microstructure before and after Heat Treatment

Figure 5 shows the microstructure of the SLMed and HTed GH3536 alloy. There were many micro-cracks and pores in the SLMed specimens. The cracks were mainly due to the large stress generated during the SLM process. The pores were due to the rapid melting and solidification such that the gas cannot be removed in time. The morphology of the molten pool formed under the action of laser beam scanning could be seen in the low-magnification structure (Figure 5a,d,g). Inside the molten pool, there were a large number of columnar crystals that were epitaxially grown perpendicular to the fusion line, as well as fine equiaxed crystals and dendrites, and the columnar crystals spanned continuously (Figure 5b,e,h). Close to the molten pool, there was an obvious “layer-to-layer” pool boundary overlap line between the melt pools, and these boundaries were distributed similarly to fish scales. Columnar crystals ran through the multilayer molten pools. Each molten pool was closely combined by metallurgical bonding, which cannot only ensure the bonding strength between the layers of the molten pool but also ensure the microstructural continuity in the growth direction. There were grains of different sizes in the structure, and the grain directions were interlaced with each other.

Figure 5c,f,i shows the high magnification of the grain boundary precipitates in the cross-section of SLMed GH3536. There were irregular near-equiaxed grains in the microstructure. At the end of the rapid solidification process of GH3536 alloy, the powder will melt into a  $\gamma$  matrix. Due to the fast solidification speed during the forming process, most of the precipitates were too late to precipitate. Carbides were precipitated at the grain boundaries of the microstructure in the alloy. Carbon was the main forming element of carbides in the deposited structure of GH3536 alloy. A small number of carbides were precipitated at the grain boundaries. With the increase in carbon content, the number of carbides precipitated at the grain boundaries increases, and the morphology changes from dispersed particles to continuous chains.

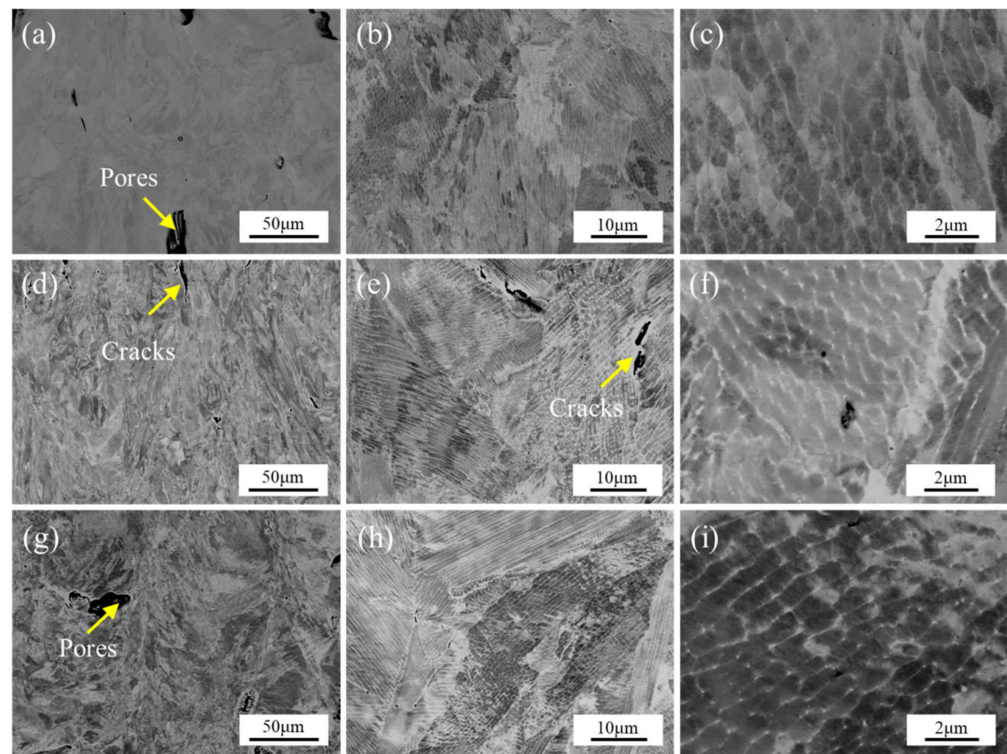


**Figure 5.** Microstructure changes before heat treatment: (a–c) transverse microstructure; (d–f) longitudinal microstructure; and (g–i) 45° microstructure.

According to the rapid solidification theory, during the rapid solidification process, the growth direction of the columnar crystals was opposite to the heat dissipation direction. During the laser melting deposition forming process, the heat was dissipated mainly downwards and outwards through the substrate and the formed parts. According to laser fusion deposition modeling, a portion of the substrate material would melt into the molten pool when the first layer was formed. The remelting depth in the middle of the cladding layer was greater than the remelting depth on both sides, forming a new molten pool. As the forming height increases, the width of the formed specimen increases with the heat build-up during the forming process. During the laser melting deposition forming process, in addition to the melting process, metallurgical reactions will also occur in the molten pool, accompanied by thermal effects, which affect the morphology of the molten pool.

The effect of heat treatment on the alloy precipitates formed by SLM was promoted. The C element determined the microstructure and mechanical properties of GH3536 alloy. When it exceeded the limit of solid solution, C would form  $M_{23}C_6$  carbides with Cr, Mo, and W. During SLM, C was also easy to segregate at the grain boundary to form carbides [25]. Carbide was a brittle phase in the alloy and reduced the material plasticity sharply, which easily led to cracks in the SLM manufacturing process. After heat treatment, the carbides in the grain boundary gradually changed from a granular distribution to a continuous strip distribution (Figure 6). There were white granular or flaky phases in the grain boundaries of the SLMed GH3536. After heat treatment, the deposited structure disappeared, the original laser scanning traces could not be observed, and recrystallization occurred. During the heat treatment process, the internal carbides were dissolved, and the internal alloying elements were homogenized.

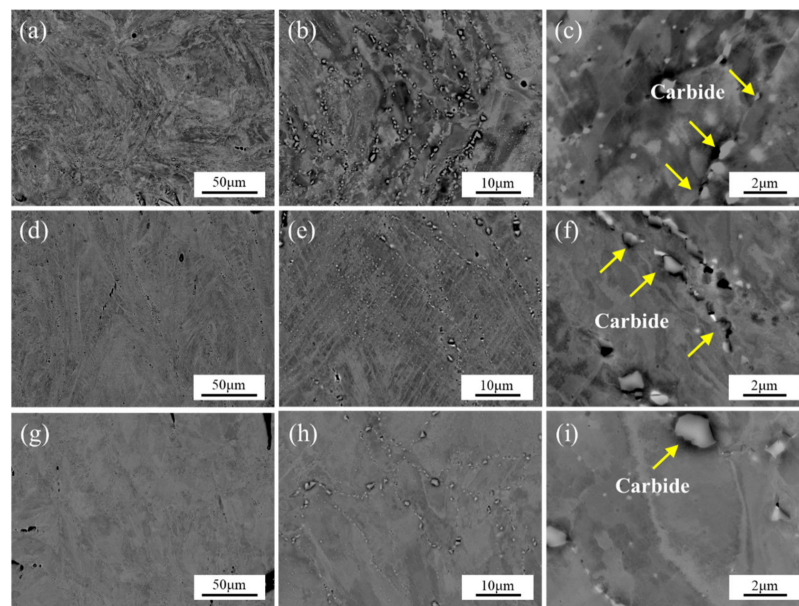


**Figure 6.** Microstructure changes after heat treatment: (a–c) transverse microstructure; (d–f) longitudinal microstructure; and (g–i) 45° microstructure.

### 3.4. Grain Characteristics before and after Heat Treatment

Figure 7 shows the EBSD results of the SLMed and HTed samples in three directions. The growth trend in all directions was gradually consistent. For the transverse samples, more than 70% of grains were below 35.0  $\mu\text{m}$  in size, and the average size was 43.2  $\mu\text{m}$ . The grain difference between longitudinal samples and 45° samples was not obvious. After heat treatment, the grain orientation changed significantly, especially for the 45° samples which gradually grew toward the (001) direction (Figure 8). In addition, the grain size gradually increased, and the average grain size was 46.8  $\mu\text{m}$  in both the transverse samples and the longitudinal samples.

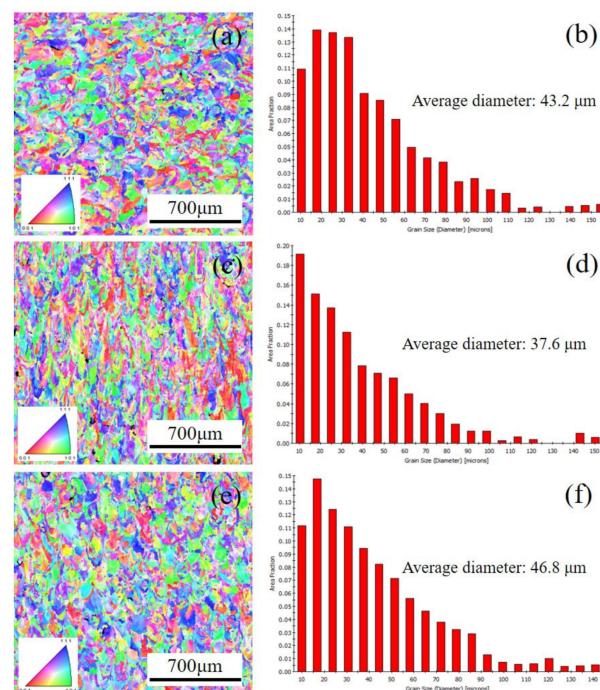


**Figure 7.** Grain orientation and size distribution of SLMed GH3536 before heat treatment: (a,b) transverse sample; (c,d) longitudinal sample; and (e,f) 45° sample.

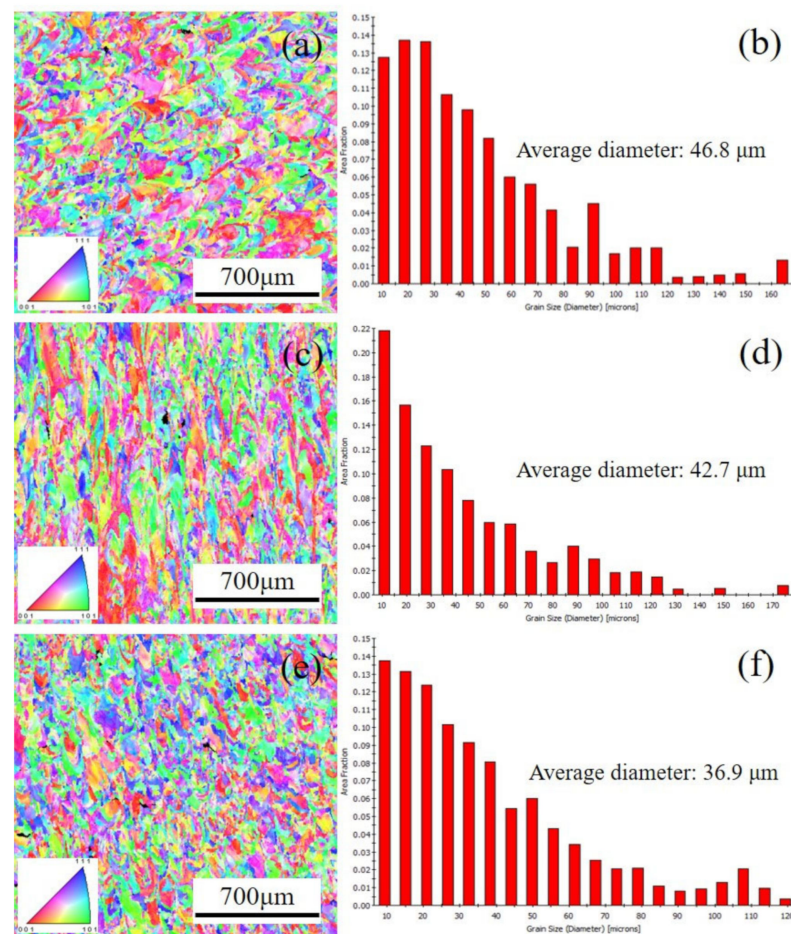
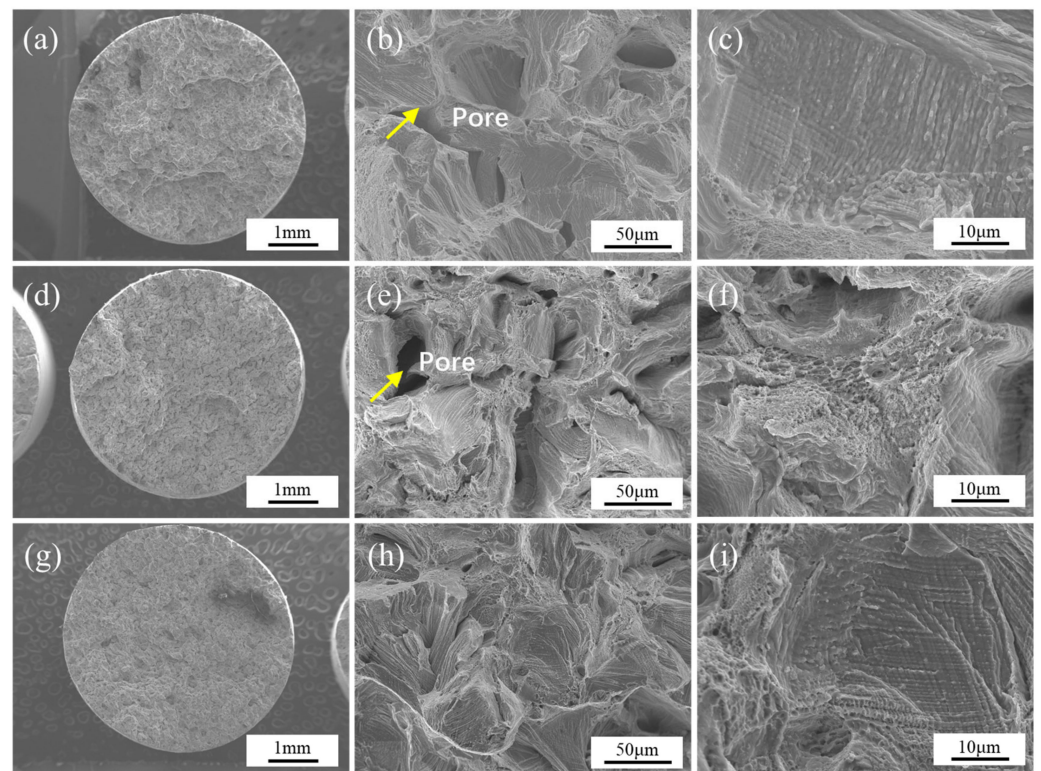


**Figure 8.** Grain orientation and size distribution of HTed GH3536 before heat treatment: (a,b) transverse sample; (c,d) longitudinal sample; and (e,f) 45° sample.

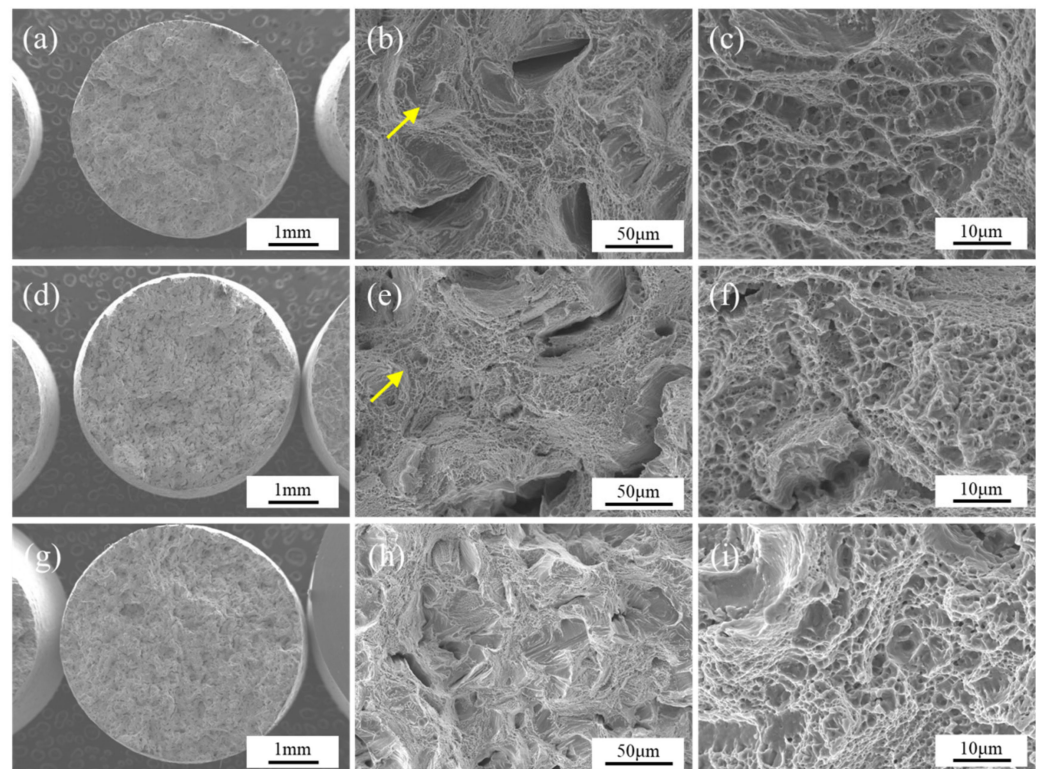
### 3.5. Fracture Morphology before and after Heat Treatment

Figure 9 is the tensile fracture morphology of the SLMed GH3536 alloy. The tensile fracture showed obvious transgranular characteristics. The scan line traces can be clearly identified on the fracture. After SLM, the GH3536 alloy sample was subjected to an external load during the tensile process; micro-pores were generated due to the fragile joint between the carbide and  $\gamma$  matrix, and along the grain, the boundary direction grew up. Tensile cracks mainly originated and propagated at the fusion line and eventually led to the fracture of samples.

The tensile fracture after heat treatment was mainly dimple morphology, and the sample had obvious plastic deformation which belonged to the ductile fracture (Figure 10). The fracture periphery was serrated, and there were a large number of secondary cracks on the outer surface of the sample. Low magnification observation showed that there were many deep holes in the section and the size of the pores was different. At high magnification, many small pores could be seen connected to form large pores. During the tensile test, the cracks in different areas initiated and grew in the form of a micro-pore aggregation until the sample broke, and the cracks in different planes expanded to form tearing edges.



**Figure 9.** Changes in tensile fracture morphology before heat treatment: (a–c) transverse sample; (d–f) longitudinal sample; and (g–i) 45° sample.



**Figure 10.** Changes in tensile fracture morphology after heat treatment: (a–c) transverse sample; (d–f) longitudinal sample; and (g–i) 45° sample.

During the high-temperature tensile process, the intragranular strength and grain boundary strength jointly determined the strength and plasticity, the amount and morphology of the intragranular precipitates determined the intragranular strength, and the morphology of the grain boundary precipitates determined grain boundary strength. Under the high-temperature environment, the fracture positions of GH3536 alloy were all intergranular fractures, and the grain boundary was the weak area (Figure 11).

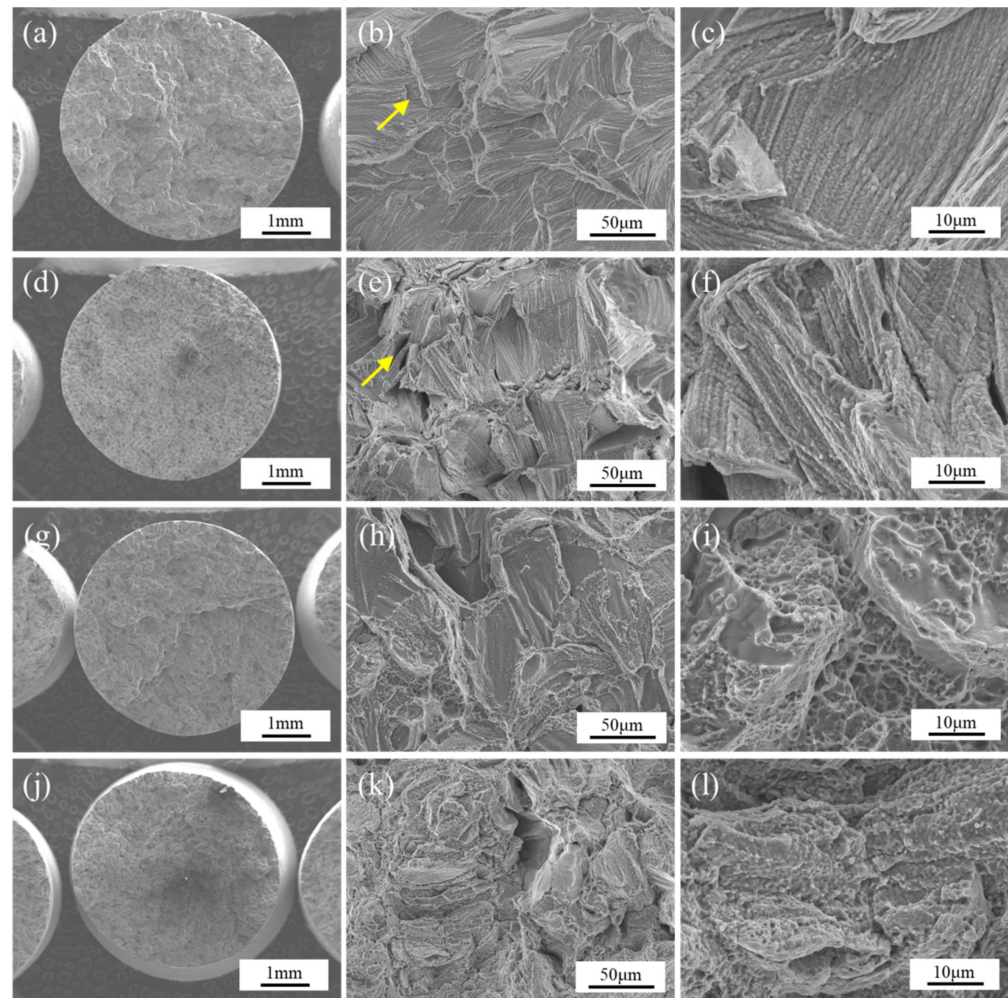


**Figure 11.** High-temperature tensile fracture before heat treatment: (a–c) transverse structure; (d–f) longitudinal structure; high-temperature tensile fracture- after heat treatment: (g–i) transverse structure; and (j–l) longitudinal structure.

#### 4. Conclusions

- (1) There are pores and cracks in the SLMed GH3536 samples, and the number in each direction did not change significantly. The tensile strength, elongation, and area reduction in transverse, 45°, and longitudinal samples increased in turn, while the yield strength did not change significantly. After heat treatment, the yield strength decreased, while the elongation increased significantly.
- (2) There were irregular near-equiaxed grains in the cross-sectional microstructure of SLMed GH3536. After heat treatment, the carbides in the grain boundary gradually changed from a granular distribution to a continuous strip distribution, and a white granular or flaky phase precipitated in the grain boundary.
- (3) The growth trend of SLMed GH3536 was gradually consistent in all directions. In the transverse samples, more than 70% of grains were below 35 µm in size. After heat treatment, the grain orientation of the 45° sample changed significantly and gradually

grew in the (001) direction. The tensile fracture of SLMed GH3536 samples changed from a transgranular fracture to a ductile fracture after heat treatment.

**Author Contributions:** Writing—review and editing, S.H.; data analysis, B.C., W.L. and S.G.; study design, B.Z. and X.Z.; Literature search, Q.Z. All authors have read and agreed to the published version of the manuscript.

**Funding:** This research and the APC was funded by the National Natural Science Foundation of China (Grant Nos. 52005465, 51875541, 52175369).

**Institutional Review Board Statement:** Not applicable.

**Informed Consent Statement:** Not applicable.

**Data Availability Statement:** Not applicable.

**Conflicts of Interest:** The authors declare no conflict of interest.

## References

1. Santos, E.C.; Shiomi, M.; Osakada, K.; Laoui, T. Rapid manufacturing of metal components by laser forming. *Int. J. Mach. Tools Manuf.* **2006**, *46*, 1459–1468. [[CrossRef](#)]
2. Li, S.; Wei, Q.; Shi, Y.; Zhu, Z.; Zhang, D. Microstructure Characteristics of Inconel 625 Superalloy Manufactured by Selective Laser Melting. *J. Mater. Sci. Technol.* **2015**, *31*, 946–952. [[CrossRef](#)]
3. Gong, G.; Ye, J.; Chi, Y.; Zhao, Z.; Wang, Z.; Xia, G.; Du, X.; Tian, H.; Yu, H.; Chen, C. Research status of laser additive manufacturing for metal: A review. *J. Mater. Res. Technol.* **2021**, *15*, 855–884. [[CrossRef](#)]
4. Bremen, S.; Meiners, W.; Diatlov, A. Selective laser melting: A manufacturing technology for the future? *Laser Tech. J.* **2012**, *9*, 33–38. [[CrossRef](#)]
5. Gu, D.D.; Meiners, W.; Wissenbach, K.; Poprawe, R. Laser additive manufacturing of metallic components: Materials, processes and mechanisms. *Int. Mater. Rev.* **2012**, *57*, 133–164. [[CrossRef](#)]
6. Chen, D.; Wang, P.; Pan, R.; Zha, C.; Fan, J.; Liang, D.; Zhao, Y. Characteristics of Metal Specimens Formed by Selective Laser Melting: A State-of-the-Art Review. *J. Mater. Eng. Perform.* **2021**, *30*, 7073–7100. [[CrossRef](#)]
7. Lai, G.Y. An investigation of the thermal stability of a commercial Ni-Cr-Fe-Mo alloy (hastelloy alloy X). *Met. Mater. Trans. A* **1978**, *9*, 827–833. [[CrossRef](#)]
8. Zhang, D.X.; Wang, J.P.; Wen, Z.X.; Liu, D.S.; Yue, Z.F. V-Notched Bar Creep Life Prediction: GH3536 Ni-Based Superalloy Under Multiaxial Stress State. *J. Mater. Eng. Perform.* **2016**, *25*, 2959–2968. [[CrossRef](#)]
9. Vieille, B.; Duchaussoy, A.; Benmabrouk, S.; Henry, R.; Keller, C. Fracture behavior of Hastelloy X elaborated by laser powder bed fusion: Influence of microstructure and building direction. *J. Alloys Compd.* **2022**, *918*, 165570. [[CrossRef](#)]
10. Cheng, Z.; Du, X.; Qi, B.; Yuan, Z.; Wu, Q.; Zou, J.; Xiao, R. Microstructure and mechanical properties of 3D-GH3536/R-GH3128 butt joint welded by fiber laser welding with focus rotation. *J. Mater. Res. Technol.* **2022**, *18*, 1460–1473. [[CrossRef](#)]
11. Zhang, H.; Xue, J.; Ye, Y.; Bai, H.; Guo, W.; Zou, G.; Liu, L. Boride evolutionary behavior and mechanism in the TLP repaired IN738 superalloy with crack-like defects. *J. Alloys Compd.* **2022**, *909*, 164692. [[CrossRef](#)]
12. Tian, Y.; Tomus, D.; Rometsch, P.; Wu, X. Influences of processing parameters on surface roughness of Hastelloy X produced by selective laser melting. *Addit. Manuf.* **2017**, *13*, 103–112. [[CrossRef](#)]
13. Ren, Y.; Li, Z.; Chen, Y.; Xin, Z.; Ye, Y.; Lu, H.; Wan, H.; Cheng, L.; He, K.; Tu, X.; et al. Effect of Heat Treatment on the Microstructure and Mechanical Properties of Nickel Superalloy GH3536 Obtained by Selective Laser Melting. *Met. Sci. Heat Treat.* **2021**, *63*, 369–374. [[CrossRef](#)]
14. Min, S.; Zhang, H.; Liu, H.; Zhang, K.; Huang, A.; Hou, J. Influence of defects on high-temperature oxidation performance of GH3536 superalloys fabricated by laser powder bed fusion. *Addit. Manuf. Lett.* **2022**, *3*, 100064. [[CrossRef](#)]
15. Wang, F. Mechanical property study on rapid additive layer manufacture Hastelloy® X alloy by selective laser melting technology. *Int. J. Adv. Manuf. Technol.* **2012**, *58*, 545–551. [[CrossRef](#)]
16. Tomus, D.; Tian, Y.; Rometsch, P.A.; Heilmaier, M.; Wu, X. Influence of post heat treatments on anisotropy of mechanical behaviour and microstructure of Hastelloy-X parts produced by selective laser melting. *Mater. Sci. Eng. A* **2016**, *667*, 42–53. [[CrossRef](#)]
17. Zhang, L.; Song, J.; Wu, W.; Gao, Z.; He, B.; Ni, X.; Long, Q.; Lu, L.; Zhu, G. Effect of processing parameters on thermal behavior and related density in GH3536 alloy manufactured by selective laser melting. *J. Mater. Res.* **2019**, *34*, 1405–1414. [[CrossRef](#)]
18. Qiao, G.; Zhang, B.; Bai, Q.; Dilnoza, Y. Effect of Heat Treatment on Microstructure and Residual Stress of GH3536 Superalloy Fabricated by Selective Laser Melting. *J. Mater. Eng. Perform.* **2021**, *30*, 8892–8900. [[CrossRef](#)]
19. Xia, Y.; Chen, H.; Liang, X.; Lei, J. Circular oscillating laser melting deposition of nickel-based superalloy reinforced by WC: Microstructure, wear resistance and electrochemical properties. *J. Manuf. Process.* **2021**, *68*, 1694–1704. [[CrossRef](#)]
20. Montero-Sistiaga, M.L.; Pourbabak, S.; Van Humbeeck, J.; Schryvers, D.; Vanmeensel, K. Microstructure and mechanical properties of Hastelloy X produced by HP-SLM (high power selective laser melting). *Mater. Des.* **2019**, *165*, 107598. [[CrossRef](#)]

21. Han, Q.; Gu, Y.; Setchi, R.; Lacan, F.; Johnston, R.; Evans, S.L.; Yang, S. Additive manufacturing of high-strength crack-free Ni-based Hastelloy X superalloy. *Addit. Manuf.* **2019**, *30*, 100919. [[CrossRef](#)]
22. Wang, H.; Chen, L.; Dovgvy, B.; Xu, W.; Sha, A.; Li, X.; Tang, H.; Liu, Y.; Wu, H.; Pham, M.-S. Micro-cracking, microstructure and mechanical properties of Hastelloy-X alloy printed by laser powder bed fusion: As-built, annealed and hot-isostatic pressed. *Addit. Manuf.* **2021**, *39*, 101853. [[CrossRef](#)]
23. Sanchez-Mata, O.; Muñoz-Lerma, J.A.; Wang, X.; Atabay, S.E.; Shandiz, M.A.; Brochu, M. Microstructure and mechanical properties at room and elevated temperature of crack-free Hastelloy X fabricated by laser powder bed fusion. *Mater. Sci. Eng. A* **2020**, *780*, 139177. [[CrossRef](#)]
24. Sun, S.; Teng, Q.; Xie, Y.; Liu, T.; Ma, R.; Bai, J.; Cai, C.; Wei, Q. Two-step heat treatment for laser powder bed fusion of a nickel-based superalloy with simultaneously enhanced tensile strength and ductility. *Addit. Manuf.* **2021**, *46*, 102168. [[CrossRef](#)]
25. Montero-Sistiaga, M.L.; Liu, Z.; Bautmans, L.; Nardone, S.; Ji, G.; Kruth, J.-P.; Van Humbeeck, J.; Vanmeensel, K. Effect of temperature on the microstructure and tensile properties of micro-crack free hastelloy X produced by selective laser melting. *Addit. Manuf.* **2020**, *31*, 100995. [[CrossRef](#)]